

Multidimensional Mapping of Spin-Exchange Optical Pumping in Clinical-Scale Batch-Mode ^{129}Xe Hyperpolarizers

Panayiotis Nikolaou,^{*,†} Aaron M. Coffey,^{†,∞} Kaili Ranta,[‡] Laura L. Walkup,^{§,●} Brogan M. Gust,[§] Michael J. Barlow,^{||} Matthew S. Rosen,^{†,#} Boyd M. Goodson,[§] and Eduard Y. Chekmenev^{*,†,∞,◇}

[†]Department of Radiology, Vanderbilt University Institute of Imaging Science (VUIIS), Nashville, Tennessee 37232, United States

[‡]Department of Physics, Southern Illinois University, Carbondale, Illinois 62901, United States

[§]Department of Chemistry and Biochemistry, Southern Illinois University, Carbondale, Illinois 62901, United States

^{||}Sir Peter Mansfield Magnetic Resonance Centre, University of Nottingham, Nottingham, NG7 2RD, U.K.

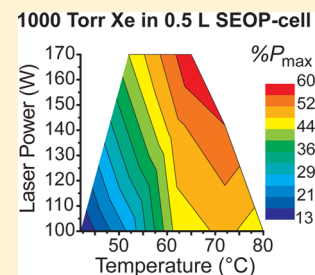
[#]Massachusetts General Hospital/Athinoula A. Martinos Center for Biomedical Imaging, Boston, Massachusetts 02129, United States

[∞]Department of Physics, Harvard University, Cambridge, Massachusetts 02138, United States

[◇]Department of Biomedical Engineering and [◇]Department of Biochemistry, Vanderbilt-Ingram Cancer Center, Nashville, Tennessee 37205, United States

Supporting Information

ABSTRACT: We present a systematic, multiparameter study of Rb/ ^{129}Xe spin-exchange optical pumping (SEOP) in the regimes of high xenon pressure and photon flux using a 3D-printed, clinical-scale stopped-flow hyperpolarizer. In situ NMR detection was used to study the dynamics of ^{129}Xe polarization as a function of SEOP-cell operating temperature, photon flux, and xenon partial pressure to maximize ^{129}Xe polarization (P_{Xe}). P_{Xe} values of $95 \pm 9\%$, $73 \pm 4\%$, $60 \pm 2\%$, $41 \pm 1\%$, and $31 \pm 1\%$ at 275, 515, 1000, 1500, and 2000 Torr Xe partial pressure were achieved. These P_{Xe} polarization values were separately validated by ejecting the hyperpolarized ^{129}Xe gas and performing low-field MRI at 47.5 mT. It is shown that P_{Xe} in this high-pressure regime can be increased beyond already record levels with higher photon flux and better SEOP thermal management, as well as optimization of the polarization dynamics, pointing the way to further improvements in hyperpolarized ^{129}Xe production efficiency.



INTRODUCTION

The nuclear spins of xenon and other noble gases can be hyperpolarized (HP) to order unity by the process of spin-exchange optical pumping (SEOP).^{1,2} In this two-step process, the electron spins of an alkali metal vapor such as rubidium are first polarized by the absorption of angular momentum from circularly polarized light. Spin-exchange collisions between the alkali metal atoms and ^{129}Xe then transfer the angular momentum to the ^{129}Xe nuclear spins through Fermi hyperfine interactions, resulting in a high non-Boltzmann distribution of ^{129}Xe spin states that increases the detection sensitivity of NMR/MRI.^{3–6} The two most common approaches to hyperpolarize ^{129}Xe via SEOP are termed *continuous flow*^{7–14} and *stopped flow*^{15–25} (sometimes also referred to as “batch mode”) with respect to the delivery of Xe gas to and from the polarization cell. N_2 gas is typically added to the gas mixture to quench alkali metal fluorescence.^{7,26,27} The batch-mode/stopped-flow systems are attractive not only because of their relative simplicity but also because they can operate in a xenon-rich regime that obviates the need to separate the polarized Xe from the N_2 (or He) via cryocollection, eliminating a potential source of polarization loss²⁸ as well as facilitating applications using quadrupolar noble gas isotopes.⁵ This production method

has also been scaled up for automated production of clinically required quantities.^{24,29,30}

Regardless of the polarization method, HP noble gases have seen wide application varying from fundamental physics experiments^{31–34} to NMR/MRI applications including molecular biosensors,^{35–37} probing structural aspects of cage molecules and proteins,^{18,38–42} and studies of porous materials (to name only a few).^{15,43–45} However, it has been biomedical applications that have largely driven the development of hyperpolarized MR techniques over the past decade; indeed, for gas imaging in particular, HP ^{129}Xe can be used to assess lung function and report on functional and microstructural abnormalities.^{6,46–48} A useful figure of merit for ^{129}Xe hyperpolarizers is the total ^{129}Xe magnetization, M_{Xe} , delivered in a clinically useful gas volume, typically $\sim 0.5\text{--}1\text{ L}$ at 760 Torr. M_{Xe} is determined by the product of nuclear spin polarization P_{Xe} and ^{129}Xe concentration [Xe], i.e., $M_{\text{Xe}} \propto P_{\text{Xe}}[\text{Xe}]$. It is therefore important to maximize M_{Xe} through both P_{Xe} and [Xe], which is challenging because P_{Xe} generally decreases as [Xe] within the SEOP-cell increases¹⁰ (mostly because of

Received: February 11, 2014

Revised: April 14, 2014

Published: April 14, 2014

increased alkali metal spin-destruction rates from non-spin-conserving collisions with Xe).^{49,50} But fundamentally laser photons are the source of ¹²⁹Xe hyperpolarization; thus, the decreasing cost of laser diodes narrowly tuned to the alkali metal rubidium D₁ wavelength (794.8 nm)⁵¹ has made economically feasible the higher photon fluxes required to improve M_{Xe} when Xe partial pressures are high.

In the present work, a 200 W laser diode array (LDA) was used in a 3D-printed, automated ¹²⁹Xe polarizer²⁹ to study SEOP dynamics as a function of xenon density, laser power, and SEOP-cell temperature. More specifically, the SEOP polarization conditions at several partial pressures of natural abundance Xe (26.44% ¹²⁹Xe isotope enrichment) were studied: (i) 275 Torr Xe and 1725 Torr N₂, (ii) 515 Torr Xe and 1485 Torr N₂, (iii) 1000 Torr Xe and 1000 Torr N₂, (iv) 1500 Torr Xe and 500 Torr N₂, and (v) 2000 Torr Xe and 200 Torr N₂, where the gases were loaded with an accuracy of ± 25 Torr. The reader is also directed to Supporting Information for detailed descriptions of the experimental setup, which represents the second-generation device of our HXTC consortium (Figure 1).^{24,30} For each SEOP cell loading, data were obtained for a range of incident laser power levels (approximately 100, 125, 140, or 170 W) and variable SEOP-cell surface temperatures ranging from 42 to 92 °C. For each condition, measurement of ¹²⁹Xe polarization dynamics allowed the rate constant for P_{Xe} accumulation (γ_{SEOP}) and the maximum attainable steady-state P_{Xe} value [$P_{\text{Xe}}(t \rightarrow \infty)$ or ¹²⁹Xe P_{max}] to be determined from exponential fits. The temperature of the SEOP cell was monitored by a thermistor mounted directly to its surface; temperature control allows the Rb concentration in the gas phase to be varied.^{52,53}

METHODS

Spin-Exchange Optical Pumping (SEOP) Polarizer. The SEOP 3D-printed portable polarizer (Figure 1) consists of a 200 W frequency narrowed volume holographic grating (VHG) laser diode array (LDA), a custom 3D-printed thermoelectric cooling (TEC) optical pumping (OP) oven, a 0.5 L SEOP cell, an electromagnet providing 47 kHz ¹²⁹Xe and ¹H Larmor frequencies, in situ NMR polarimetry endowed by a Magritek Kea2 system, and a Magritek 88 mm bore magnet for ex situ NMR polarimetry and MRI (Magritek, Wellington, New Zealand). The components of the polarizer²⁹ and 47.5 mT MRI⁵⁴ have been discussed in detail previously²⁹ and thus are only discussed briefly here.

In Situ Low-Field NMR and IR Spectroscopy. In situ NMR polarimetry for these experiments was performed via single-shot ¹²⁹Xe NMR at 47 kHz (Figure 2a) calibrated against ¹H NMR at the same frequency from a sample of thermally polarized water doped with 10 mM CuSO₄ inside a 0.5 L SEOP-cell phantom (200 000 scans, Figure 2b). The polarizer allows the Rb electron spin polarization, P_{Rb} , to be estimated by comparing the integrated intensities of transmitted laser spectra measured with and without the applied magnetic field (e.g., Figure 2c).^{19,24} For each set of conditions, P_{Xe} was sampled every 5–20 min throughout SEOP; the process is repeated by either destroying the ¹²⁹Xe polarization with a series of “crusher” pulses or allowing it to decay with the laser off. The time-course examples in Figure 2d,e show the excellent reproducibility of P_{Xe} , P_{Rb} , and γ_{SEOP} in these experiments (and those values were not sensitive to the application of the rf pulses). Once steady-state ¹²⁹Xe polarization was achieved,

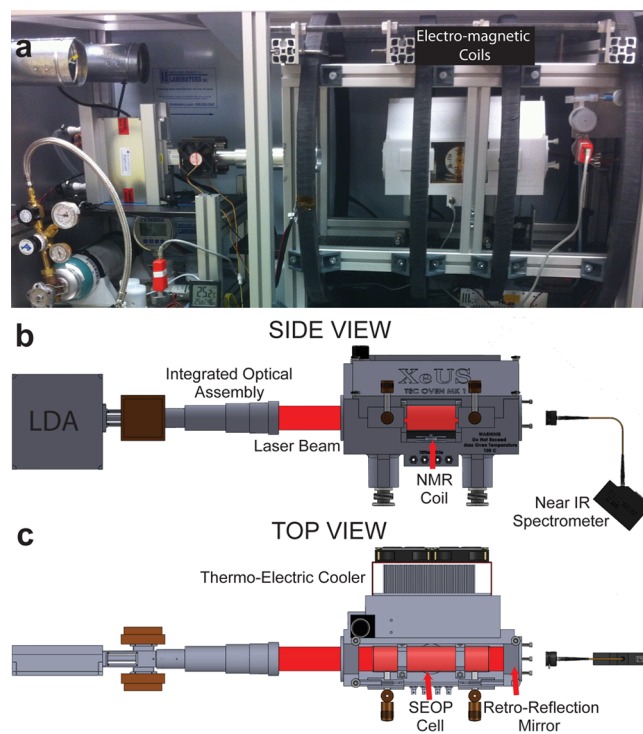


Figure 1. (a) Spin exchange optical pumping (SEOP) 3D-printed polarizer used to perform all in situ experiments. (b) Side view of laser aligned to the SEOP oven, SEOP cell, and near-IR spectrometer. (c) Top view, with the oven lid removed to show SEOP cell.²⁹

growth curves can be extracted (e.g., Figure 2f) and fit to an exponential: $P_{\text{Xe}}(t) = P_{\text{max}}[1 - \exp(-\gamma_{\text{SEOP}}t)]$. In the absence of SEOP, in-cell room-temperature (rt) measurement of the spin-lattice relaxation time constant (T_1) can be obtained after steady-state P_{Xe} has been achieved by quickly bringing the cell to room temperature to minimize the Rb gas-phase concentration, turning off the laser, and performing in situ NMR polarimetry while the polarization decays; for example, the data in Figure 2g were fit to an exponential decay curve: $P_{\text{Xe}}(t) = P_{\text{Xe}}(0) \exp[-\Gamma_{\text{Xe}} t]$, where Γ_{Xe} ($=1/T_1$) is the ¹²⁹Xe spin-destruction rate, here exhibiting an ultralong in-cell ¹²⁹Xe T_1 of 150.5 ± 2.5 min (or 2.5 h). Particularly when optimizing SEOP under the regimes of high [Xe] and laser power, it is also important to be observant for the onset of positive feedback effects that give rise to dramatic increases in [Rb] and laser absorption over time (and ultimately poorer P_{Xe}). Examples showing the manifestation of such “Rb-runaway”⁵⁵ effects are provided in Figure 2h, which shows behavior where relatively small increases in cell surface temperature result not only in reduced peak P_{Xe} but also in reduced P_{Xe} over time. Such effects are discussed in greater detail in Results and Discussion.

Ex Situ Low-Field NMR Spectroscopy and MRI Imaging. Ex situ P_{Xe} at 47.5 mT was calculated by comparing the HP ¹²⁹Xe signal with the ¹³C signal at 508 kHz ¹³C Larmor frequency from a reference sample of thermally polarized sodium ¹³C-acetate dissolved in D₂O (Figure 4a). The ¹²⁹Xe T_1 relaxation time inside the polypropylene phantom sphere was ~ 9.2 min (Figure 4c), which is sufficient for short-term storage of HP ¹²⁹Xe. Moreover, this ¹²⁹Xe T_1 value was used in parallel experiments to precisely calibrate the rf excitation pulse for the 47.5 mT rf probe shown in Figure 5f; the image signal decay is due to both T_1 decay and excitation rf pulses. A y-slice

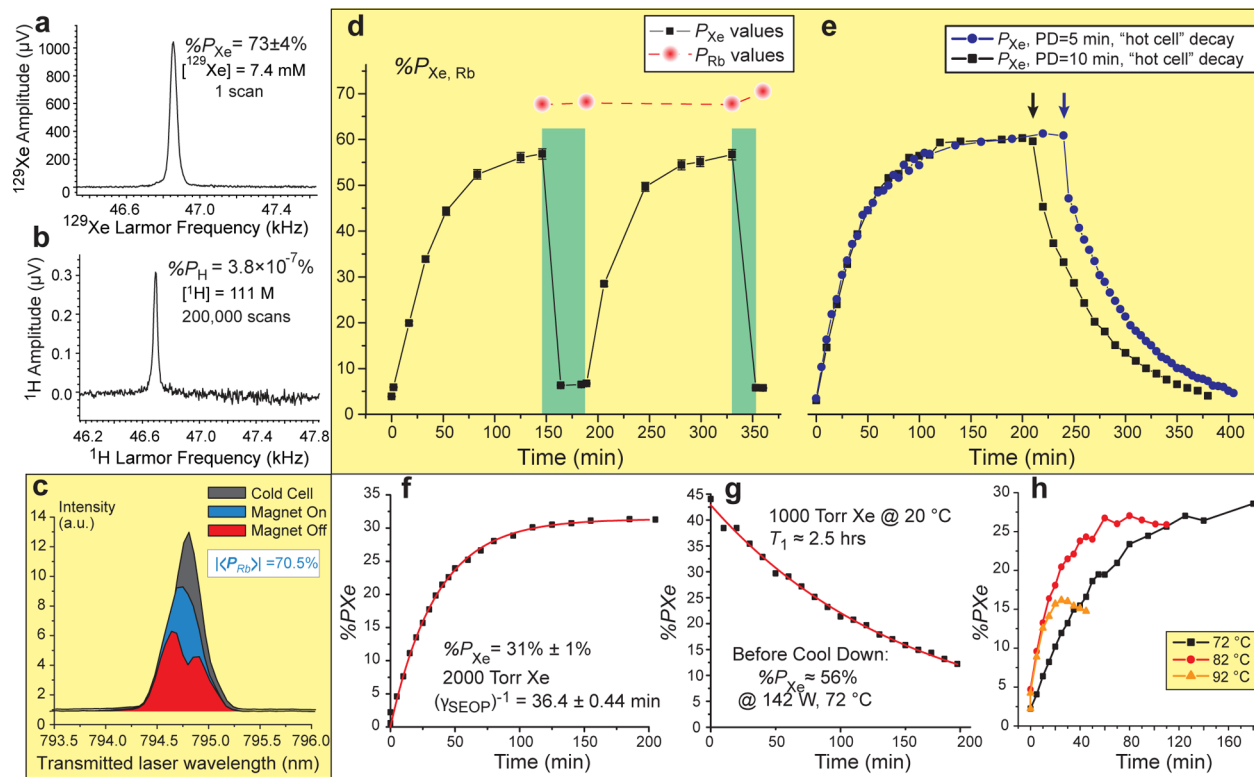


Figure 2. (a) Example of an in situ low-field ^{129}Xe NMR spectrum from a SEOP-cell during SEOP (single scan, $B_0 = 4.00 \text{ mT}$). (b) Corresponding ^1H NMR spectrum from a thermally polarized water reference sample using 200 000 scans, $B_0 = 1.10 \text{ mT}$. (c) Examples of field-cycled near-IR spectra of laser light transmitted through the SEOP-cell used to estimate P_{Rb} : room temperature before SEOP (dark gray), during SEOP with B_0 electromagnet on (blue), and during SEOP with B_0 electromagnet turned off (red). (d, e) Examples of data sets for studying time-resolved SEOP build-up and decay kinetics using a cell containing 1000 Torr (each) of Xe and N₂ gas (143 W laser power, 65 °C). (d) Plot showing reproducibility of P_{Xe} accumulation following the application of >500 rf “crusher” pulses that nearly zero-out the ^{129}Xe polarization (time periods marked by vertical green bars); P_{Rb} (red circles) was sampled via field-cycled near-IR spectroscopy (c) before and after application of the crusher pulses. (e) Similar to (d), with ^{129}Xe NMR signals acquired with different interpulse durations and with polarization decay observed after turning the laser off (times demarcated with vertical arrows); here ^{129}Xe decay was observed with the SEOP cell temperature maintained at 65 °C. Pulse delay (PD) refers to timing between NMR acquisitions during build-up. (f) Exponential buildup of ^{129}Xe polarization during the SEOP process for a cell filled with 2000 Torr of Xe and 200 Torr of N₂. (g) T_1 decay of HP ^{129}Xe at r.t. obtained with the laser turned off. (h) Time-course examples showing the temperature-dependent effects of nonequilibrium “Rb runaway”^{9,51,55} in a 1500 Torr Xe SEOP cell using only 100 W laser power: a normal build-up curve at 72 °C (black squares), a mildly distorted build-up curve at 82 °C (red circles), and a significantly distorted build-up curve at 92 °C (orange triangles). All spectra were recorded with a surface coil using small radiofrequency (rf) excitation pulses with little to no measurable effect on ^{129}Xe magnetization. Except for the fitting curves in (f) and (g), connecting lines are meant only to guide the eye.

projection of fast gradient echo (GRE) imaging with millimeter-scale spatial resolution without slice selection shows the excellent ^{129}Xe signal intensity (Figure 5a). All 20 images (Figure 5b–e, selected images shown) were acquired identically with TE = 4.0 ms, TR ≈ 80 ms (limited by the spectrometer electronics response time), 50% k -space sampling, 64 × 64 imaging matrix with 72 × 72 mm² field of view (FOV), and a spectral width of 20 kHz. Given the relatively long T_1 in the phantom (Figure 4c), the decay of the hyperpolarized signal was primarily due to rf-pulse-induced polarization loss in Figure 5f. The calibrated rf pulse width for the flip angle ($2.7^\circ \pm 0.1^\circ$) was used for calculation of % P_{Xe} for the HP ^{129}Xe post-transfer in Figure 4 (see Supporting Information for details).

RESULTS AND DISCUSSION

The dependence of ^{129}Xe polarization and its dynamics as functions of temperature, photon flux, and xenon partial pressure was systematically studied under stopped-flow operation in the regimes of high xenon density and photon flux. Results for five Xe:N₂ SEOP-cell compositions at four different LDA incident powers (approximately 100, 125, 140,

and 170 W) with SEOP-cell surface temperatures ranging from 42 to 92 °C are displayed in Figure 3: Figure 3a provides example plots of % P_{max} and γ_{SEOP} as functions of SEOP-cell surface temperature for a cell containing 1000 Torr of Xe and 1000 Torr of N₂ and illuminated by 100 W of laser power from the LDA. Such data were used to create contour plots (“maps”) of ^{129}Xe % P_{max} and γ_{SEOP} for each Xe density as functions of laser power and SEOP-cell surface temperature (Figures 3c–l); the highest values achieved for % P_{max} for each Xe:N₂ mix studied are summarized in Figure 3b and Table 1 (corresponding numerical values for all data points in Figure 3 are tabulated in the Supporting Information, Table S1).

The data in Figure 3 exhibit several trends. First, increasing cell surface temperature gives rise to an exponential increase in γ_{SEOP} (e.g., Figure 3a), consistent with the expected exponential increase in the Rb gas-phase concentration [Rb].^{52,53} This dependence of γ_{SEOP} on [Rb] arises from the relation^{1,2}

$$\gamma_{\text{SEOP}} = \gamma_{\text{SE}} + \Gamma_{\text{Xe}} = k_{\text{SE}}[\text{Rb}] + \Gamma_{\text{Xe}} \quad (1)$$

where γ_{SE} and k_{SE} are the Rb/ ^{129}Xe spin-exchange rate and cross-section, respectively. Thus, the behavior of γ_{SEOP} mostly

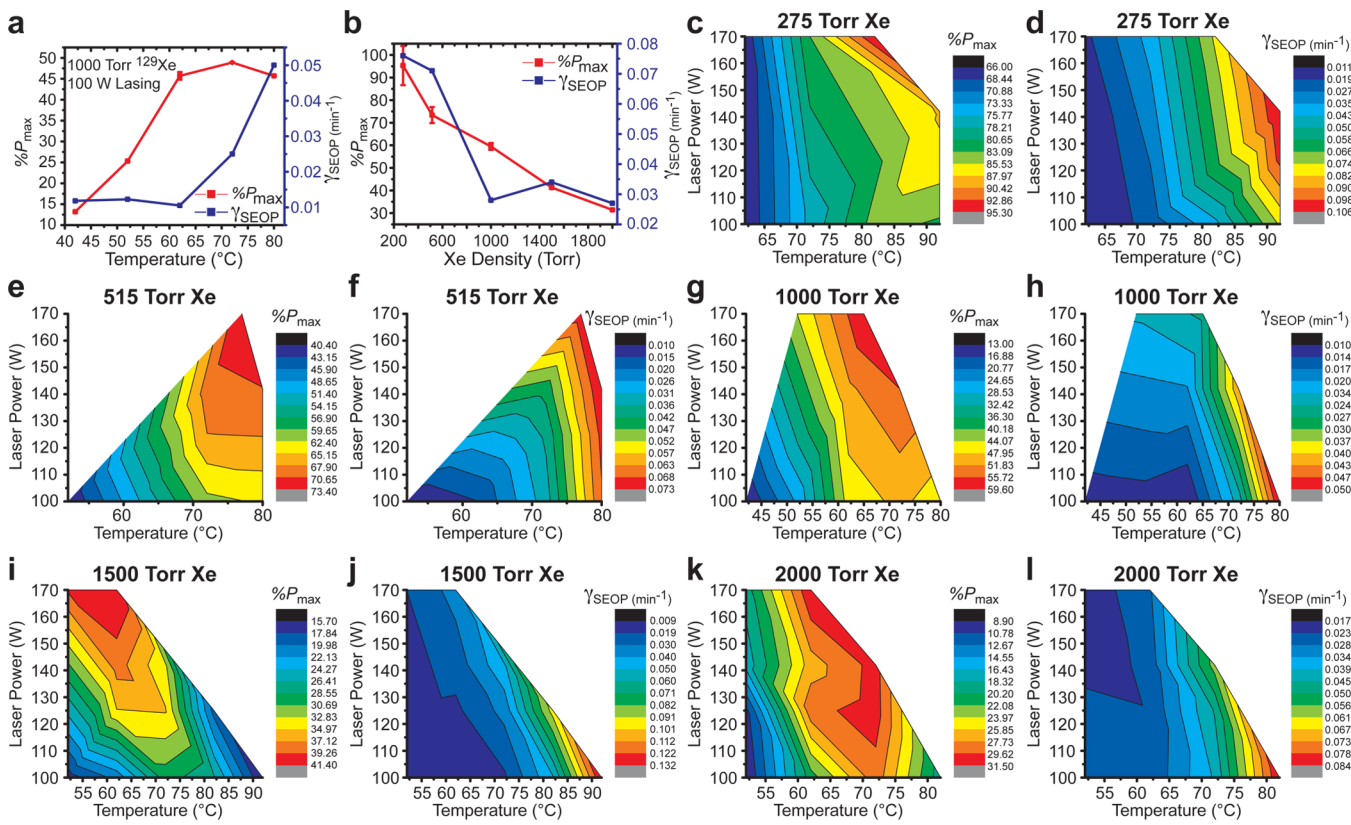


Figure 3. Mapping the conditions of Rb/¹²⁹Xe SEOP for five different Xe partial pressures. (a) Example data set showing the dependence of % P_{\max} and γ_{SEOP} on the SEOP-cell surface temperature, here for a 1000 Torr Xe pressure cell (also filled with 1000 Torr N₂) with 100 W incident laser power. (b) Dependence of % P_{\max} and γ_{SEOP} on Xe partial pressure for five cell Xe:N₂ compositions using 170 W incident laser power and operating at the optimal cell temperature for each Xe loading. (c-l) % P_{\max} and γ_{SEOP} maps for five cell Xe:N₂ compositions showing the interdependence on incident laser power and SEOP-cell surface temperature.

reflects the spin-exchange rate, since generally $k_{\text{SE}}[\text{Rb}] > \Gamma_{\text{Xe}}$ or $k_{\text{SE}}[\text{Rb}] \gg \Gamma_{\text{Xe}}$ under our conditions. (At the highest temperatures studied, $k_{\text{SE}}[\text{Rb}] \gg \Gamma_{\text{Xe}}$; at the lowest temperatures $k_{\text{SE}}[\text{Rb}]$ can approach or become less than Γ_{Xe} , but Γ_{Xe} is expected to have a more mild dependence on surface temperature that trends in the opposite direction.⁵⁶)

However, P_{\max} exhibits significantly different behavior, for example, peaking at ~72 °C for the data in Figure 3a. P_{\max} is given by

$$P_{\max} = \frac{k_{\text{SE}}[\text{Rb}]}{k_{\text{SE}}[\text{Rb}] + \Gamma_{\text{Xe}}} \langle P_{\text{Rb}} \rangle \quad (2)$$

where $\langle P_{\text{Rb}} \rangle$ is the spatial average of the local Rb electron spin polarization, $P_{\text{Rb}}(r)$, which itself is determined by

$$P_{\text{Rb}}(r) = \frac{\gamma_{\text{OP}}(r)}{\gamma_{\text{OP}}(r) + \Gamma_{\text{Rb}}} \quad (3)$$

where $\gamma_{\text{OP}}(r)$ is the local Rb optical pumping rate (the integrated product of the laser flux at position r and the Rb absorption cross section) and Γ_{Rb} is the Rb electronic spin destruction rate (which is essentially proportional to [Xe] under our conditions^{49,50}). Intuitively from eq 2, ¹²⁹Xe $P_{\max} \rightarrow \langle P_{\text{Rb}} \rangle$ when $k_{\text{SE}}[\text{Rb}] \gg \Gamma_{\text{Xe}}$, which occurs at higher temperatures. However, having higher Rb densities generally translates into greater optical density, which in turn gives rise to reduced transmittance of the laser light and hence poorer illumination throughout the cell, lower γ_{OP} , and ultimately reduced $\langle P_{\text{Rb}} \rangle$, thereby decreasing P_{\max} . Thus, % P_{\max} initially grows with

increasing temperature as more Rb is vaporized (e.g., Figure 3a), but once [Rb] becomes too high, overall $\langle P_{\text{Rb}} \rangle$ decreases in accordance with eq 3, resulting in lower ¹²⁹Xe % P_{\max} at some of the highest temperatures studied.

The highest % P_{\max} values in the contour plots of Figure 3c–l were always achieved at the maximum LDA power of 170 W. However, as the Xe density increased, the optimal temperature decreased from 92 to 62 °C, in qualitative agreement with our previous results obtained at a much smaller scale.^{21,51} This inverse relationship between Xe density and optimal cell surface temperature, an effect amplified by the use of frequency-narrowed lasers,²² may be explained in part by the fact that as [Xe] rises, Xe-induced Rb spin-destruction becomes increasingly dominant; thus, lowering the cell temperature helps maintain a sufficient “photon-to-Rb” ratio to ensure high global $\langle P_{\text{Rb}} \rangle$ and hence higher % P_{\max} (provided that the cell ¹²⁹Xe T_1 is sufficiently long²⁴). The effect may also be exacerbated by greater in-cell temperature gradients caused by (i) greater absorption of laser energy and (ii) the several-fold lower thermal conductivity of Xe compared to that of N₂.^{57,58} Indeed, the effects of differential heating are also manifested in the γ_{SEOP} maps: γ_{SEOP} (and hence γ_{SE}) is not a constant of exterior cell temperature but shows some variation. For example, the value at 100 W, 82 °C for the 2000 Torr Xe gas composition is nearly twice that for the 275 Torr Xe gas composition; overall, apparent γ_{SEOP} values tend to increase with increasing laser power and [Xe], consistent with higher-than-expected Rb vapor densities (and higher internal temperatures) under these conditions.

Table 1. Summary of Maximum ^{129}Xe % P_{\max} , M'_{Xe} ($M'_{\text{Xe}} = (\% P)(C_{129\text{Xe}})$), and Other ^{129}Xe Hyperpolarizer Metrics Achieved for Five Gas Mixtures^a

Xe/N ₂ partial pressure (Torr)	$C_{129\text{Xe}}$ (mM)	% $P_{\text{Xe}}(\max)$ (%)	% $P_{\text{Xe}}(\max,\text{app})$ (%)	$M'_{\text{Xe}}(\max)$ (mM)	production cycle time (min)	apparent production rate (L/h)
275/1725	3.9	95 ± 9	13 ± 1	3.7 ± 0.3	51	0.94
515/1485	7.4	73 ± 4	19 ± 1	5.4 ± 0.3	53	0.91
1000/1000	14.3	60 ± 2	30 ± 1	8.5 ± 0.3	98	0.49
1500/500	21.4	41 ± 1	31 ± 1	8.8 ± 0.2	84	0.57
2000/200	28.6	31 ± 1	28 ± 1	9.0 ± 0.2	98	0.49

^aApparent or usable ^{129}Xe hyperpolarization % $P_{\max}(\text{app})$ is computed according to ref 23 to reflect that ^{129}Xe is diluted by N₂ gas as follows: % $P_{\text{Xe}}(\max,\text{app}) = [\% P_{\text{Xe}}(\max)](p_{\text{Xe}}/p_{\text{tot}})$ where p_{Xe} is partial pressure of Xe and p_{tot} is total mixture pressure. The production cycle time (for producing of ~0.8 L of HP $^{129}\text{Xe}/\text{N}_2$ gas mix) is calculated as the sum of $2/\gamma_{\text{SEOP}}$ (i.e., when the bulk (87% of P_{\max}) of ^{129}Xe hyperpolarization is established, in addition to a reasonable (25 min long) interval necessary to unload/reload the OP cell (with cool-down/reheating procedure described in ref 24) with xenon mix; γ_{SEOP} value corresponding to a maximum value of % P_{\max} was used for every gas composition. The production rate is calculated by dividing ~0.8 L gas volume expanded in the Tedlar bag during each production cycle by the production cycle time.

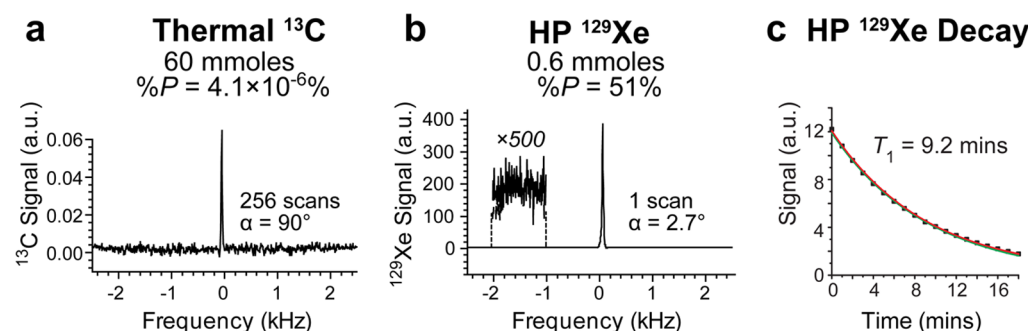


Figure 4. Ex situ 47.5 mT NMR spectroscopy of HP ^{129}Xe gas expanded into a phantom. (a) ^{13}C NMR spectroscopy using thermal ^{13}C polarization ($\% P_{13\text{C}} = 4.1 \times 10^{-6}\%$) of a 17.5 mL reference sample of 5.2 g of sodium $1\text{-}^{13}\text{C}$ -acetate dissolved in D₂O. 256 averages were acquired at 508 kHz resonance frequency with a 90° square excitation rf pulse and a repetition time (TR) of 200 s. Acquisition time was 100 ms. (b) Ex situ ^{129}Xe NMR spectroscopy of HP ^{129}Xe gas ejected from the polarizer, 0.61 mmol of ^{129}Xe spins ($\% P_{\text{Xe}} = 51 \pm 2\%$); cell loading was 1000 Torr of Xe and 1000 N₂. The spectrum is acquired at 558.6 kHz ^{129}Xe resonance frequency with a single scan (2.7° excitation rf pulse) and TR = 200 ms. The rf pulse is calibrated by monitoring signal decay in the MRI images (see Figure 5) and accounting for T_1 relaxation of the HP ^{129}Xe in the phantom (c).

Next, there is a clear indication that all the studied Xe densities benefited from the increased laser power (see also Figure S1). Consequently, the use of LDA power greater than 170 W should lead to further increases in % P_{\max} . Furthermore, if the increased heat load could be mitigated, greater LDA power would allow for operation in the regimes with higher [Rb], thereby increasing γ_{SEOP} and HP ^{129}Xe production rate.

Data are absent from some regions of the SEOP maps in Figures 3c–l. These regions were avoided because the build-up rate γ_{SEOP} was found to be excessively long, the % P_{\max} values were clearly low, and/or the conditions would render an unfavorably high [Rb], resulting in undesirable effects dubbed “Rb pre-runaway” or “Rb runaway”. The phenomenon of “Rb runaway” takes place when undissipated heat from laser absorption or cell heating rapidly compounds the amount of Rb in the vapor phase over a short time;^{9,21} the increasing [Rb] results in decreasing P_{Rb} in more poorly illuminated regions of the cell and hence more laser absorption and heat dissipation from the gas into the inner surface of the cell (and Rb pools) in a self-reinforcing pattern. The effect can be characterized by its severity: In full Rb runaway, one sees a dramatic decrease in the amount of laser light transmitted through the cell over time which may be followed by deteriorating P_{Xe} and even elevated exterior cell surface temperatures. The behavior is also hysteretic, as simple temperature reduction to normal operating regimes generally fails to regain efficient SEOP. On the other hand, a more mild condition (here termed “Rb pre-runaway”) does not have as pronounced a manifestation in the transmitted

laser’s near-IR spectroscopy but is readily observed during measurements of the kinetics of P_{Xe} build-up. Examples of “Rb pre-runaway” can be seen in Figure 2h (orange trace), where P_{Xe} grows, passes the maximum, and then dips. The effect is less pronounced in Figure 2h (red trace) and nonobservable in Figure 2h (black trace). While true “Rb runaway” causes % P_{Xe} to irreversibly deteriorate and requires a restart of the SEOP procedure from initial conditions to lower [Rb], “Rb pre-runaway” is not hysteretic and can be more easily controlled by reducing the cell temperature. However, it results in lower polarization (Figure 2h). In any case, these deleterious effects are more problematic for higher Xe densities because of the greater Rb spin-destruction rates (and hence greater light absorption from more poorly polarized Rb, as well as any possible contributions from reduced thermal conductivity).

Table 1 summarizes the maximum achieved ^{129}Xe polarization (% P_{\max}) for every Xe:N₂ mix studied. The results show not only the trend of decreased % P_{\max} with increasing Xe in-cell pressure but also a corresponding decrease in γ_{SEOP} measured at these optimal conditions, a finding that predominantly reflects the lower concentration of Rb vapor that must be attained to achieve maximal ^{129}Xe polarization at higher Xe densities. Nevertheless, the optimization process allows the total magnetization (M'_{Xe}) to continue to grow despite the decrease in % P_{\max} ²¹ as the ^{129}Xe density increases faster than % P_{\max} decreases. While the ^{129}Xe polarization values (and amounts) are significantly higher here than those in ref 21, the improvement in M'_{Xe} from 1000 to 2000 Torr of Xe is

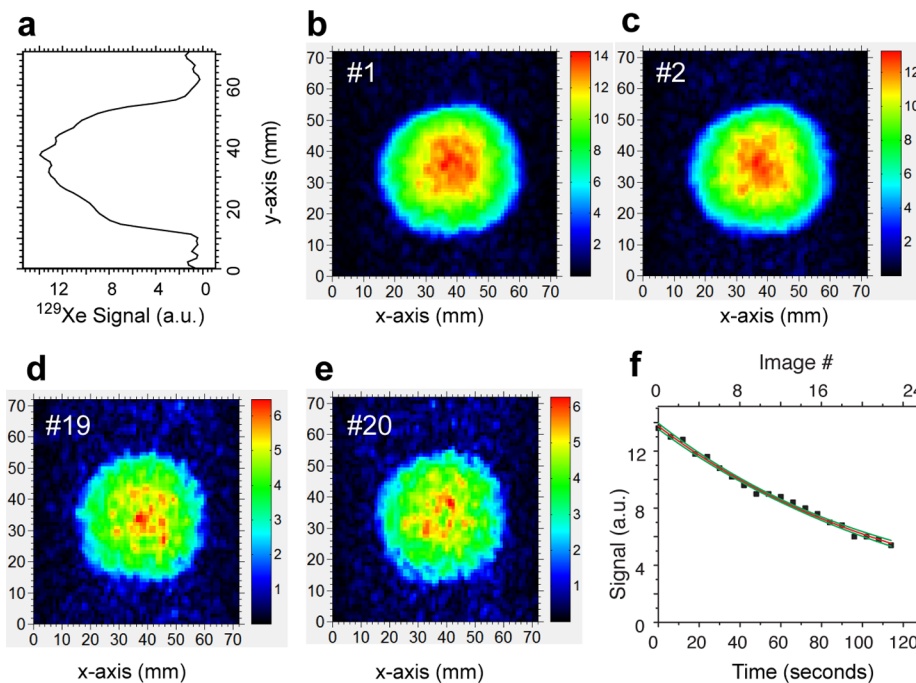


Figure 5. Hyperpolarized ¹²⁹Xe gas MRI at 47.5 mT. (a) *y*-slice/projection across the center of the image shown in (b). (b–e) Selected MRI gradient echo (GRE) images from a series of 20 images. All 20 images were acquired identically with TE = 4.0 ms, TR ≈ 80 ms (limited by the spectrometer electronics response time), 50% *k*-space sampling, 64 × 64 imaging matrix with 72 × 72 mm² field of view (FOV), and a spectral width of 20 kHz. (f) Decay of HP signal primarily due to rf-pulse-induced polarization loss. The temporal decay of the signal measured between individual images within 20-image series was used to calibrate rf pulse width ($2.7^\circ \pm 0.1^\circ$ corresponding to 20 μ s at \sim 80 mW) using T_1 determined by the data shown in Figure 4c, because the signal decay in Figure 5f is due to both T_1 decay and excitation rf-pulse-associated magnetization losses.

more marginal. Higher laser power may provide further improvements in % P_{max} (and M'_{Xe}) at high [Xe] by allowing operation with higher Rb densities and hence higher γ_{SEOP} rates. Other useful metrics describing the overall hyperpolarizer performance summarized in Table 1 include the apparent % $P_{\text{Xe}}(\text{max})$ due to Xe dilution by N₂ gas (% $P_{\text{Xe}}(\text{max,app})$), production cycle time, and apparent production rate of hyperpolarized gas (L/h). % $P_{\text{Xe}}(\text{max,app})$ is a useful metric²³ because it takes into account HP Xe dilution by N₂ gas, which has not been eliminated because the HP Xe cryocollection step was obviated. Production cycle time corresponds to the time necessary to complete the production of \sim 0.8 L of HP Xe/N₂ gas composition and return the hyperpolarizer (i.e., gas reloading, etc.) to the same step in the operational cycle. Computed in this fashion production cycle time was used for estimating the apparent production rate of the hyperpolarizer in liters of hyperpolarized Xe/N₂ mixture per hour. The production rate in L/h is truly the characteristic of continuous-flow hyperpolarizers, and the apparent production rate values computed in Table 1 should be used with care for direct comparison with continuous-flow hyperpolarizers, because the batch-mode method used here produces a single batch per each production cycle, and there is no produced HP ¹²⁹Xe until the cycle is finished.

To validate the *in situ* NMR results, the polarized contents of the SEOP-cell filled with 1000 Torr of Xe and 1000 Torr of N₂ was transferred into an evacuated ($<10^{-3}$ Torr) 0.05 L hollow polypropylene sphere located in a rf probe of a 47.5 mT imaging system^{54,59,60} (see Supporting Information for details). In-cell P_{Xe} was measured *in situ* as $54 \pm 5\%$ before the transfer, and a P_{Xe} value of $51 \pm 2\%$ was detected in the 47.5 mT preclinical MRI scanner (558.6 kHz ¹²⁹Xe Larmor frequency),

corresponding to polarization enhancement $\varepsilon > 11\,000\,000$ after the gas transfer (Figure 4b). The HP ¹²⁹Xe transfer from the polarizer was performed without a cryocollection process.^{24,25,30} Figure 5 also demonstrates the feasibility of millimeter-scale MRI of hyperpolarized ¹²⁹Xe at very low magnetic fields using frequency optimized rf coils.⁵⁴

CONCLUSIONS

Simultaneous optimization of various SEOP conditions (Xe density, cell surface temperature, and photon flux) combined with previously reported SEOP hardware improvements^{24,29,30} yielded greatly improved % P_{Xe} . Indeed, very high values of % P_{Xe} and M'_{Xe} were demonstrated here for dense (up to 2000 Torr of Xe in 2200 Torr total) Xe gas mixtures, in part enabled by optimized laser illumination throughout the cell, ultralong in-cell ¹²⁹Xe relaxation times, and efficient thermal management that also allows for diligent avoidance of “Rb runaway” regimes. The SEOP condition maps provide guidance for the production of highly polarized ¹²⁹Xe gas at different xenon densities for a wide variety of applications ranging from materials science to biomedical imaging. Furthermore, our results indicate that the P_{Xe} values at higher Xe densities are still laser-power-limited. Thus, while the benefit in total Xe magnetization was less substantial at the highest Xe densities studied, the advantage will likely be improved when more powerful LDA instrumentation is available provided that the greater thermal loads can be mitigated. Finally, the highly reproducible maps of γ_{SEOP} build-up rates, combined with automated fine control of cell conditions and real-time spectroscopic feedback, should also allow optimization of multiexponential Xe polarization dynamics, pointing the way to multifold improvements in HP ¹²⁹Xe production efficiency.

■ ASSOCIATED CONTENT

● Supporting Information

Detailed information regarding the SEOP setup used, the preparation processes, and experimental parameters. This material is available free of charge via the Internet at <http://pubs.acs.org>.

■ AUTHOR INFORMATION

Corresponding Authors

*P.N.: (phone) 615-203-6912; (fax) 615-322-0734; (e-mail) peter.nikolaou@vanderbilt.edu.

*E.Y.C.: (address) Department of Radiology, Vanderbilt University Institute of Imaging Science, Nashville, TN 37232; (phone) 615-322-1329; (fax) 615-322-0734; (e-mail) eduard.chekmenev@vanderbilt.edu.

Present Address

●L.L.W.: Cincinnati Children's Hospital Medical Center, Cincinnati, OH.

Notes

The authors declare no competing financial interest.

■ ACKNOWLEDGMENTS

Work at Vanderbilt and SIUC is supported by a DoD CDMRP Era of Hope Award W81XWH-12-1-0159/BC112431. Portions of this work were supported by SIU Office of Sponsored Projects Administration (OSPA). B.M.G. is supported in part by the NIH (Grant 2R15EB007074-02). E.Y.C. is supported in part by the NIH (Grant 3R00CA134749-03). M.J.B. acknowledges the support of the School of Medicine, University of Nottingham, U.K. M.S.R. acknowledges the support of Department of Defense, Defense Medical Research, and Development Program, Applied Research and Advanced Technology Development Award, Grant W81XWH-11-2-0076 (DM09094).

■ REFERENCES

- (1) Walker, T. G.; Happer, W. Spin-Exchange Optical Pumping of Noble-Gas Nuclei. *Rev. Mod. Phys.* **1997**, *69* (2), 629–642.
- (2) Walker, T. G. Fundamentals of Spin-Exchange Optical Pumping. *J. Phys.: Conf. Ser.* **2011**, *294*, 012001.
- (3) Goodson, B. M. Nuclear Magnetic Resonance of Laser-Polarized Noble Gases in Molecules, Materials, and Organisms. *J. Magn. Reson.* **2002**, *155* (2), 157–216.
- (4) Bifone, A.; Cherubini, A. Hyperpolarised Xenon in Biology. *Prog. Nucl. Magn. Reson. Spectrosc.* **2003**, *42* (1–2), 1–30.
- (5) Lilburn, D.; Pavlovskaya, G. E.; Meersmann, T. Perspectives of Hyperpolarized Noble Gas MRI Beyond ^3He . *J. Magn. Reson.* **2012**, *229*, 173–186.
- (6) Mugler, J. P.; Altes, T. A. Hyperpolarized ^{129}Xe MRI of the Human Lung. *J. Magn. Reson. Imaging* **2013**, *37* (2), 313–331.
- (7) Driehuys, B.; Cates, G. D.; Miron, E.; Sauer, K.; Walter, D. K.; Happer, W. High-Volume Production of Laser-Polarized Xe-129 . *Appl. Phys. Lett.* **1996**, *69* (12), 1668–1670.
- (8) Haake, M.; Pines, A.; Reimer, J. A.; Seydoux, R. Surface-Enhanced NMR Using Continuous-Flow Laser-Polarized Xenon. *J. Am. Chem. Soc.* **1997**, *119*, 11711–11712.
- (9) Zook, A. L.; Adhyaru, B. B.; Bowers, C. R. High Capacity Production of >65% Spin Polarized Xenon-129 for NMR Spectroscopy and Imaging. *J. Magn. Reson.* **2002**, *159* (2), 175–182.
- (10) Mortuza, M. G.; Anala, S.; Pavlovskaya, G. E.; Dieken, T. J.; Meersmann, T. Spin-Exchange Optical Pumping of High-Density Xenon-129. *J. Chem. Phys.* **2003**, *118* (4), 1581–1584.
- (11) Knagge, K.; Prange, J.; Raftery, D. A Continuously Recirculating Optical Pumping Apparatus for High Xenon Polarization and Surface NMR Studies. *Chem. Phys. Lett.* **2004**, *397*, 11–16.
- (12) Ruset, I. C.; Ketel, S.; Hersman, F. W. Optical Pumping System Design for Large Production of Hyperpolarized Xe-129 . *Phys. Rev. Lett.* **2006**, *96* (5), 053002.
- (13) Schrank, G.; Ma, Z.; Schoeck, A.; Saam, B. Characterization of a Low-Pressure High-Capacity Xe-129 Flow-Through Polarizer. *Phys. Rev. A* **2009**, *80* (6), No. 063424.
- (14) Norquay, G.; Parnell, S. R.; Xu, X.; Parra-Robles, J.; Wild, J. M. Optimized Production of Hyperpolarized ^{129}Xe at 2 Bar for in Vivo Lung Magnetic Resonance Imaging. *J. Appl. Phys.* **2013**, *113*, No. 044908.
- (15) Raftery, D.; Long, H.; Meersmann, T.; Grandinetti, P. J.; Reven, L.; Pines, A. High-Field NMR of Adsorbed Xenon Polarized by Laser Pumping. *Phys. Rev. Lett.* **1991**, *66*, 584–587.
- (16) Rosen, M. S.; Chupp, T. E.; Coulter, K. P.; Welsh, R. C.; Swanson, S. D. Polarized ^{129}Xe Optical Pumping/Spin Exchange and Delivery System for Magnetic Resonance Spectroscopy and Imaging Studies. *Rev. Sci. Instrum.* **1999**, *70* (2), 1546–1552.
- (17) Ruth, U.; Hof, T.; Schmidt, J.; Fick, D.; Jansch, H. J. Production of Nitrogen-Free, Hyperpolarized ^{129}Xe Gas. *Appl. Phys. B: Lasers Opt.* **1999**, *68* (1), 93–97.
- (18) Desvaux, H.; Gautier, T.; Le Goff, G.; Petro, M.; Berthault, P. Direct Evidence of a Magnetization Transfer between Laser-Polarized Xenon and Protons of a Cage-Molecule in Water. *Eur. Phys. J. D* **2000**, *12* (2), 289–296.
- (19) Nikolaou, P.; Whiting, N.; Eschmann, N. A.; Chaffee, K. E.; Goodson, B. M.; Barlow, M. Generation of Laser-Polarized Xenon Using Fiber-Coupled Laser Diode Arrays Narrowed with Integrated Volume Holographic Gratings. *J. Magn. Reson.* **2009**, *197* (2), 249–254.
- (20) Parnell, S. R.; Deppe, M.; Parra-Robles, J.; Wild, J. M. Enhancement of ^{129}Xe Polarization by Off-Resonant Spin Exchange Optical Pumping. *J. Appl. Phys.* **2010**, *108*, 064908.
- (21) Whiting, N.; Nikolaou, P.; Eschmann, N. A.; Barlow, M. J.; Goodson, B. M. Interdependence of Xenon Density and Temperature on $\text{Rb}/^{129}\text{Xe}$ Optical Pumping Efficiency at High Xenon Densities. *J. Magn. Reson.* **2011**, *208* (2), 298–304.
- (22) Whiting, N.; Eschmann, N. A.; Barlow, M. J.; Goodson, B. M. $^{129}\text{Xe/Cs}$ (D1, D2) versus $^{129}\text{Xe/Rb}$ (D1) Spin-Exchange Optical Pumping at High Xenon Densities Using High-Power Laser Diode Arrays. *Phys. Rev. A* **2011**, *83* (5), 053428.
- (23) Six, J.; Hughes-Riley, T.; Stupic, K.; Pavlovskaya, G.; Meersmann, T. Pathway to Cryogen Free Production of Hyperpolarized Krypton-83 and Xenon-129. *PLoS One* **2012**, *7*, e49927.
- (24) Nikolaou, P.; Coffey, A. M.; Walkup, L. L.; Gust, B. M.; Whiting, N.; Newton, H.; Barcus, S.; Muradyan, I.; Dabaghyan, M.; Moroz, G. D.; et al. Near-Unity Nuclear Polarization with an “Open-Source” ^{129}Xe Hyperpolarizer for NMR and MRI. *Proc. Natl. Acad. Sci. U.S.A.* **2013**, *110* (35), 14150–14155.
- (25) Hughes-Riley, T.; Six, J. S.; Lilburn, D. M. L.; Stupic, K. F.; Dorke, A. C.; Shaw, D. E.; Pavlovskaya, G. E.; Meersmann, T. Cryogenics Free Production of Hyperpolarized ^{129}Xe and ^{83}Kr for Biomedical MRI Applications. *J. Magn. Reson.* **2013**, *237* (0), 23–33.
- (26) Saha, I.; Nikolaou, P.; Whiting, N.; Goodson, B. M. Characterization of Violet Emission from Rb Optical Pumping Cells Used in Laser-Polarized Xenon NMR Experiments. *Chem. Phys. Lett.* **2006**, *428* (4–6), 268–276.
- (27) Walter, D. K.; Griffith, W. M.; Happer, W. Energy Transport in High-Density Spin-Exchange Optical Pumping Cells. *Phys. Rev. Lett.* **2001**, *86*, 3264–3267.
- (28) Kuzma, N. N.; Patton, B.; Raman, K.; Happer, W. Fast Nuclear Spin Relaxation in Hyperpolarized Solid Xe-129 . *Phys. Rev. Lett.* **2002**, *88*, 147602.
- (29) Nikolaou, P.; Coffey, A. M.; Walkup, L. L.; Gust, B.; LaPierre, C.; Koehnemann, E.; Barlow, M. J.; Rosen, M. S.; Goodson, B. M.; Chekmenev, E. Y. A 3D-Printed High Power Nuclear Spin Polarizer. *J. Am. Chem. Soc.* **2014**, *136* (4), 1636–1642.

- (30) Nikolaou, P.; Coffey, A. M.; Walkup, L. L.; Gust, B. M.; Whiting, N. R.; Newton, H.; Muradyan, I.; Dabaghyan, M.; Ranta, K.; Moroz, G.; et al. XeNA: An Automated “Open-Source” ^{129}Xe Hyperpolarizer for Clinical Use. *Magn. Reson. Imaging* **2014**, *32*, 541–550.
- (31) Friar, J. L.; Gibson, B. F.; Payne, G. L.; Bernstein, A. M.; Chupp, T. E. Neutron Polarization in Polarized He-3 Targets. *Phys. Rev. C* **1990**, *42* (6), 2310–2314.
- (32) Anthony, P. L.; Arnold, R. G.; Band, H. R.; Borel, H.; Bosted, P. E.; Breton, V.; Cates, G. D.; Chupp, T. E.; Dietrich, F. S.; Dunne, J.; et al. Determination of the Neutron Spin Structure–Function. *Phys. Rev. Lett.* **1993**, *71* (7), 959–962.
- (33) Romalis, M. V.; Ledbetter, M. P. Transverse Spin Relaxation in Liquid Xe-129 in the Presence of Large Dipolar Fields. *Phys. Rev. Lett.* **2001**, *87* (6), 067601.
- (34) Morgan, S. W.; Fine, B. V.; Saam, B. Universal Long-Time Behavior of Nuclear Spin Decays in a Solid. *Phys. Rev. Lett.* **2008**, *101*, 067601.
- (35) Spence, M. M.; Rubin, S. M.; Dimitrov, I. E.; Ruiz, E. J.; Wemmer, D. E.; Pines, A.; Yao, S. Q.; Tian, F.; Schultz, P. G. Functionalized Xenon as a Biosensor. *Proc. Natl. Acad. Sci. U.S.A.* **2001**, *98* (19), 10654–10657.
- (36) Schroder, L.; Lowery, T. J.; Hilty, C.; Wemmer, D. E.; Pines, A. Molecular Imaging Using a Targeted Magnetic Resonance Hyperpolarized Biosensor. *Science* **2006**, *314* (5798), 446–449.
- (37) Meldrum, T.; Seim, K. L.; Bajaj, V. S.; Palaniappan, K. K.; Wu, W.; Francis, M. B.; Wemmer, D. E.; Pines, A. A Xenon-Based Molecular Sensor Assembled on an MS2 Viral Capsid Scaffold. *J. Am. Chem. Soc.* **2010**, *132* (17), 5936–5937.
- (38) Song, Y. Q.; Goodson, B. M.; Taylor, R. E.; Laws, D. D.; Navon, G.; Pines, A. Selective Enhancement of NMR Signals for Alpha-Cyclodextrin with Laser-Polarized Xenon. *Angew. Chem., Int. Ed. Engl.* **1997**, *36* (21), 2368–2370.
- (39) Rubin, S. M.; Spence, M. M.; Goodson, B. M.; Wemmer, D. E.; Pines, A. Evidence of Nonspecific Surface Interactions between Laser-Polarized Xenon and Myoglobin in Solution. *Proc. Natl. Acad. Sci. U.S.A.* **2000**, *97* (17), 9472–9475.
- (40) Rubin, S. M.; Spence, M. M.; Pines, A.; Wemmer, D. E. Characterization of the Effects of Nonspecific Xenon–Protein Interactions on Xe-129 Chemical Shifts in Aqueous Solution: Further Development of Xenon as a Biomolecular Probe. *J. Magn. Reson.* **2001**, *152* (1), 79–86.
- (41) Dubois, L.; Da Silva, P.; Landon, C.; Huber, J. G.; Ponchet, M.; Vovelle, F.; Berthault, P.; Desvaux, H. Probing the Hydrophobic Cavity of Lipid Transfer Protein from Nicotiana Tabacum through Xenon-Based NMR Spectroscopy. *J. Am. Chem. Soc.* **2004**, *126* (48), 15738–15746.
- (42) Huber, G.; Beguin, L.; Desvaux, H.; Brotin, T.; Fogarty, H. A.; Dutasta, J. P.; Berthault, P. Cryptophane–Xenon Complexes in Organic Solvents Observed through NMR Spectroscopy. *J. Phys. Chem. A* **2008**, *112* (45), 11363–11372.
- (43) Meersmann, T.; Logan, J. W.; Simonutti, R.; Caldarelli, S.; Comotti, A.; Sozzani, P.; Kaiser, L. G.; Pines, A. Exploring Single-File Diffusion in One-Dimensional Nanochannels by Laser-Polarized Xe-129 NMR Spectroscopy. *J. Phys. Chem. A* **2000**, *104* (50), 11665–11670.
- (44) Nossov, A.; Haddad, E.; Guenneau, F.; Mignon, C.; Gedeon, A.; Gross, D.; Babonneau, F.; Bonhomme, C.; Sanchez, C. The First Direct Probing of Porosity on Supported Mesoporous Silica Thin Films through Hyperpolarised Xe-129 NMR. *Chem. Commun.* **2002**, *21*, 2476–2477.
- (45) Jansch, H. J.; Gerhard, P.; Koch, M. Xe-129 on Ir(111): NMR Study of Xenon on a Metal Single Crystal Surface. *Proc. Natl. Acad. Sci. U.S.A.* **2004**, *101* (38), 13715–13719.
- (46) Patz, S.; Hersman, F. W.; Muradian, I.; Hrovat, M. I.; Ruset, I. C.; Ketel, S.; Jacobson, F.; Topulos, G. P.; Hatabu, H.; Butler, J. P. Hyperpolarized Xe-129 MRI: A Viable Functional Lung Imaging Modality? *Eur. J. Radiol.* **2007**, *64* (3), 335–344.
- (47) Mugler, J. P.; Altes, T. A.; Ruset, I. C.; Dregely, I. M.; Mata, J. F.; Miller, G. W.; Ketel, S.; Ketel, J.; Hersman, F. W.; Ruppert, K. Simultaneous Magnetic Resonance Imaging of Ventilation Distribution and Gas Uptake in the Human Lung Using Hyperpolarized Xenon-129. *Proc. Natl. Acad. Sci. U.S.A.* **2010**, *107* (50), 21707–21712.
- (48) Wild, J.; Marshall, H.; Xu, X.; Norquay, G.; Parnell, S.; Clemence, M.; Griffiths, P.; Parra-Robles, J. Simultaneous Imaging of Lung Structure and Function with Triple-Nuclear Hybrid MR Imaging. *Radiology* **2013**, *267*, 251–255.
- (49) Nelson, I. A.; Walker, T. G. Rb-Xe Spin Relaxation in Dilute Xe Mixtures. *Phys. Rev. A* **2001**, *65*, 012712.
- (50) Bouchiat, M. A.; Brossel, J.; Pottier, L. C. Evidence for Rb-Rare-Gas Molecules from the Relaxation of Polarized Rb Atoms in a Rare Gas. Experimental Results. *J. Chem. Phys.* **1972**, *56*, 3703–3714.
- (51) Whiting, N.; Nikolaou, P.; Eschmann, N. A.; Goodson, B. M.; Barlow, M. J.; Lammert, R.; Ungar, J.; Vaissie, L. Using Frequency-Narrowed, Tunable Laser Diode Arrays with Integrated Volume Holographic Gratings for Rb/ ^{129}Xe Spin-Exchange Optical Pumping at High Resonant Laser Fluxes and High Xenon Densities. *Appl. Phys. B: Lasers Opt.* **2012**, *106* (4), 775–788.
- (52) Steck, D. A. Alkali D Line Data: Rubidium 85 and 87 D Line Data. <http://steck.us/alkalidata> (accessed May 15, 2013).
- (53) Alcock, C. B.; Itkin, V. P.; Horrigan, M. K. Vapor Pressure Equations for the Metallic Elements: 298–2500 K. *Can. Metall. Q.* **1984**, *23*, 309.
- (54) Coffey, A. M.; Truong, M. L.; Chekmenev, E. Y. Low-Field MRI Can Be More Sensitive Than High-Field MRI. *J. Magn. Reson.* **2013**, *237*, 169–174.
- (55) Witte, C.; Kunth, M.; Rossella, F.; Schröder, L. Observing and Preventing Rubidium Runaway in a Direct-Infusion Xenon-Spin Hyperpolarizer Optimized for High-Resolution Hyper-Cest (Chemical Exchange Saturation Transfer Using Hyperpolarized Nuclei) NMR. *J. Chem. Phys.* **2014**, *140* (8), 084203.
- (56) Anger, B. C.; Schrank, G.; Schoeck, A.; Butler, K. A.; Solum, M. S.; Pugmire, R. J.; Saam, B. Gas-Phase Spin Relaxation of ^{129}Xe . *Phys. Rev. A* **2008**, *78* (4), 043406.
- (57) Whiting, N.; Newton, H.; Morris, P.; Barlow, M. J.; Goodson, B. M. Observation of Energy Thermalization and ~1000 K Gas Temperatures during Spin-Exchange Optical Pumping at High Xenon Densities. *Phys. Rev. A*, under review.
- (58) Kaye, G. W. C.; Laby, T. H. *Tables of Physical and Chemical Constants*; Longman: Essex, U.K., 1995; Vol. 16.
- (59) Waddell, K. W.; Coffey, A. M.; Chekmenev, E. Y. In Situ Detection of PHIP at 48 mT: Demonstration Using a Centrally Controlled Polarizer. *J. Am. Chem. Soc.* **2011**, *133* (1), 97–101.
- (60) Coffey, A. M.; Shchepin, R. V.; Wilkens, K.; Waddell, K. W.; Chekmenev, E. Y. A Large Volume Double Channel ^1H -X RF Probe for Hyperpolarized Magnetic Resonance at 0.0475 T. *J. Magn. Reson.* **2012**, *220*, 94–101.